ORIGINAL ARTICLE

lajss.org
Latin American Journal of Solids and Structures

www.lajss.org

Oblique penetration performance of Explosively Formed Projectile (EFP) on 6061 aluminum target:experiments and simulations

Yuxuan Gao[a], Chong Ji[a], Xin Wang[a]*, Yuting Wang[a], Changxiao Zhao[a]

[a] College of Field Engineering, Army Engineering University of PLA, Nanjing 210007, China. E-mails: 2099108489@qq.com, 2468645816@qq.com, 310433804@qq.com, wangyuting@njust.edu.cn, 360349734@qq.com

* Corresponding author.

https://doi.org/10.1590/1679-78257901

Abstract

In this paper, the penetration resistance of 6061 aluminum plates to explosively formed projectiles (EFPs) at the incidence angles of 0°, 15°, 30°, and 45° was studied. The penetration process was roughly divided into three typical stages—the plastic flanging stage of the target, the righting stage of the projectile, and the plug formation stage of the target. Through the energy analysis, the energy consumption of the aluminum plate increased with the increase in the incidence angle during the entire penetration process. Through the microscopic analysis of the perforated wall surface of the aluminum plate, it was found that there were distinct boundaries and differences between the plastic reaming zone and the punching plug fracture zone.. Overall, four kinds of classification modes were proposed for the damage of the aftereffect plate, which provides a method to evaluate the aftereffect of EFP oblique penetration into 6061 aluminum plates.

Keywords

Blast Explosively formed projectile; 6061 aluminum; oblique penetration; reaming; aftereffect

Graphical Abstract

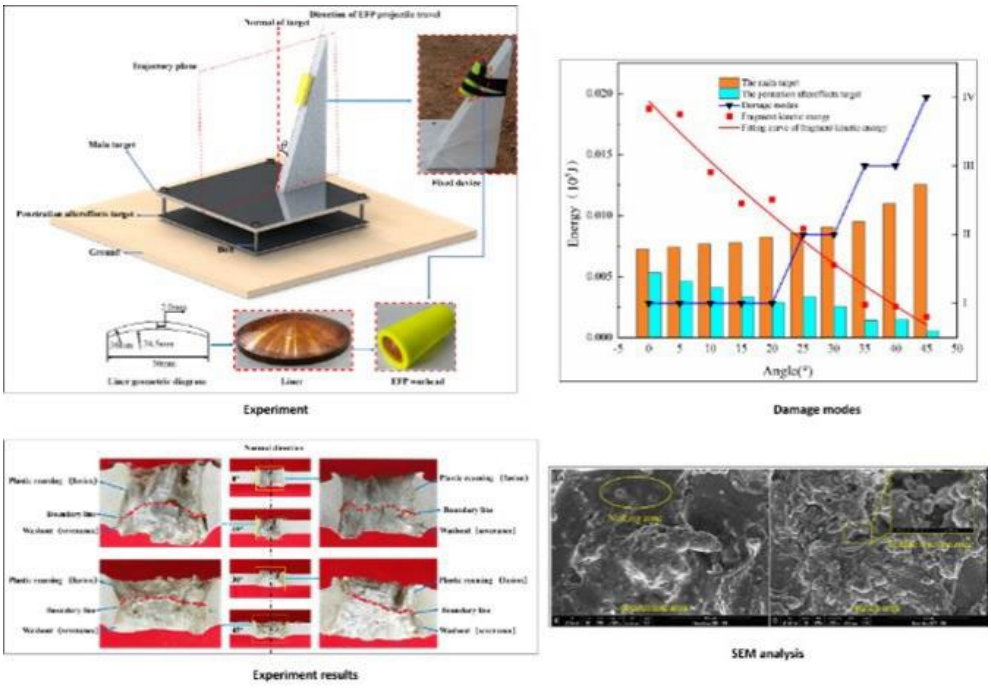

Received: November 02, 2023. In revised form: November 09, 2023. Accepted: November 14, 2023. Available online: November 21, 2023.
https://doi.org/10.1590/1679-78257901

Latin American Journal of Solids and Structures. ISSN 1679-7825. Copyright © 2023. This is an Open Access article distributed under the terms of the Creative Commons Attribution License, which permits unrestricted use, distribution, and reproduction in any medium, provided the original work is properly cited.

1 INTRUDUCTION

Compared with the armor-penetrating shaped charge jet, an explosively formed projectile (EFP) is not sensitive to the burst height, which allows the EFP to penetrate the roof of an armored vehicle. In the process of penetration, the EFP body and the metal target will be broken or eroded, and a large number of secondary fragments will be produced behind the target, which has a certain aftereffect and significantly improves the damage effect of the EFP warhead. Kurzawa (2018) selected ARMOX·370T armor steel and an EFP charge in an anti-armor mine as the research object and analyzed the dynamic plastic deformation characteristics of armor materials through metallographic inspection of the armor steel after penetration. Liu (2018,2017) carried out experiments on the impacts of EFPs on multilayer steel plates of different materials, tested and analyzed the microstructural evolution and fracture morphology characteristics of the wall surface of the bullet holes, and revealed the damage mechanism of EFP materials on the target plates. At present, most of the research on EFP penetration used a vertical approach as the initial condition, while oblique incidence is the more common approach attitude of EFPs in practice. Ji (2015) studied the responses of Q235 steel multilayer spacer targets under the oblique impacts of EFP simulants and found that the residual velocities of the EFP simulants decreased significantly with the increase in the impact inclination angle, and a large impact inclination angle could lead to ricochet of the EFP simulants. Through three-dimensional numerical simulations, Vayig (2022) explored the penetration force of a rigid ball-head projectile hitting a thick metal target at an oblique angle. The threshold bounce angle was found to depend on a dimensionless entity equal to the ratio between the penetration resistance of the target and the dynamic pressure exerted by the projectile at impact. Through the numerical derivation of the empirical relationship, it was also found that the penetration depth of the inclined ball-head rigid projectile depended on this dimensionless parameter. Cheng (2022) studied the oblique penetration of short-bar projectiles into thin metal targets and concluded that the critical ricochet velocity of the projectile increased with the increase in the penetration angle. When the angle was larger, the ultimate penetration velocity of the projectile increased sharply.

The 6061 aluminum alloy, which exhibits excellent machining performances, good corrosion resistance, high toughness, and no deformation after processing, is a dense material without defects and has other notable characteristics. It is widely used in the aerospace industry, weapon manufacturing, and equipment production (2022,2017,2022). Moreover, its dynamic characteristics under the impact of high-speed kinetic energy-penetration bodies have attracted the attention of scholars. Yadav (2022) penetrated 6061 aluminum target plates with stainless-steel flat head projectiles and confirmed that the 6061 aluminum alloy has high strength, stiffness, and impact resistance. Li (2002) carried out experiments to strengthen the resistance of 6061 aluminum composite materials and 6061 aluminum alloy materials to ultra-high-speed projectile impacts and performed microscopic analysis on the fracture morphology of the spalling zone along the crater edge in the target using scanning electron microscopy (SEM). Lee (2001) used numerical simulations to study the penetration behavior of 6061 aluminum and carbon fiber–reinforced 6061 aluminum metal matrix composite plates under tungsten bullet impacts.

From the discussion above, it can be seen that the current research on 6061 aluminum has been basically based on the resistance of metal matrix composite materials to rigid projectile penetration. Relatively little research has focused on anti-plastic projectile penetration. As typical high-pressure plastic-forming penetration bodies, EFPs will suffer from erosion, head upsetting, and other phenomena during the penetration process. Moreover, hole formation and plastic reaming will occur at the intersection of the projectile and target. In the late stage of penetration, the thin target will form a punch block. After the target, due to the formation of its own residual fragments and the punch block of the target plate, fragments of different sizes will be produced, which will have a certain aftereffect. Unfortunately, at present, there is a lack of research on the anti-EFP penetration characteristics of 6061 aluminum target plates, and their anti-penetration damage response characteristics are not clear. The mechanism through which the key factors affect the penetration behavior needs to be clarified, and there are currently no guidelines regarding the actual protection design.

Based on the above background, an experimental study of the copper EFP oblique penetration of 6061 aluminum composite targets was designed and carried out in this study, and the influences of the target angle on the macro/micro-characteristics and aftereffects of the target perforation were analyzed. A numerical model was established and validated, and a new understanding of the energy dissipation and distribution mechanism during EFP penetration was obtained. Based on the experimental and numerical simulation results, the typical damage modes of the aftereffect plate were defined, and the mapping between the modes and the EFP impact angle was established, which provides a reference method for practical protection design and damage assessment.

2 Experimental Setup

The experimental device designed in this paper for EFP oblique penetration of 6061 aluminum target plates is shown in Fig. 1. The EFP warhead was composed of a copper-powder-type cover, trinitrotoluene (TNT) explosive, and plastic shell. The liner had a variable wall thickness. The bottom diameter was 30 mm, the inner and outer curvature radii were 38.5 and 36 mm, and the top wall thickness was 2 mm. The diameter of the warhead charge was 30 mm, the height was 80 mm, and the detonation point was located at the bottom center of the charge. The shell material of the warhead was plastic resin, and its thickness was 2 mm. The impact target was composed of a front main target plate and a rear effect plate, the dimensions of which were 400 × 400 × 12 mm and 400 × 400 × 4 mm, respectively. The material was the 6061 aluminum alloy, and the distance between the two was 7.0 cm. The combined target was fixed with bolts at the corners.

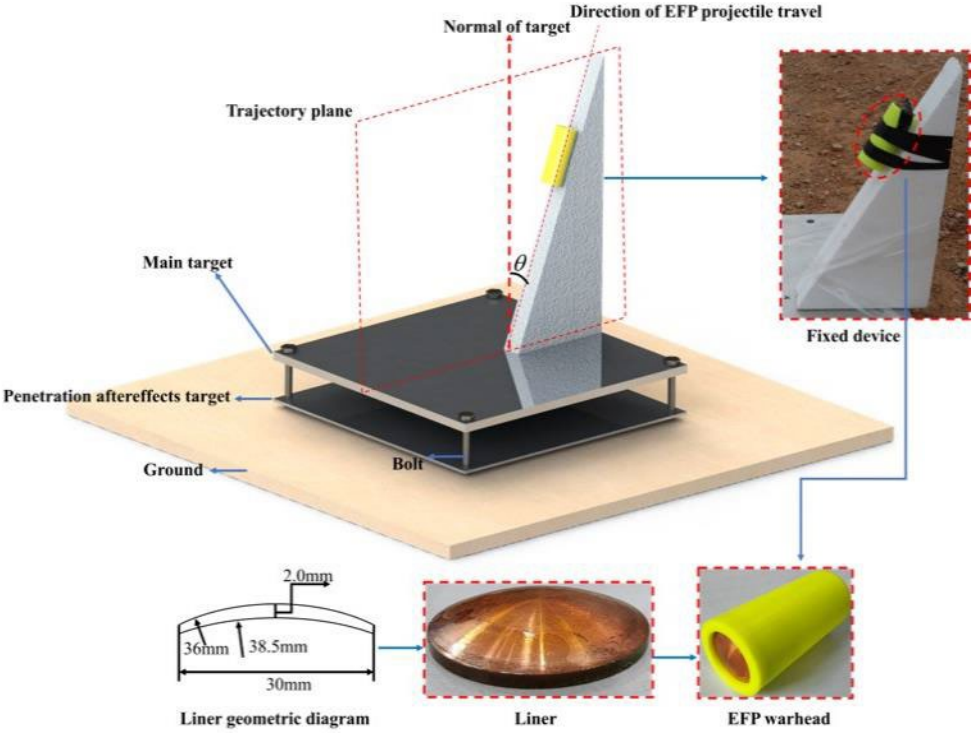

Figure 1 Experimental setup

The EFP warhead was wrapped with tape on the foam board, and the foam board was cut to the required size and angle such that the EFP oblique penetrated the target board. In order to study the influences of different incidence angles (θ) on the penetration effect, four penetration schemes with θ values of 0°, 15°, 30°, and 45° were selected, as shown in Fig. 2.

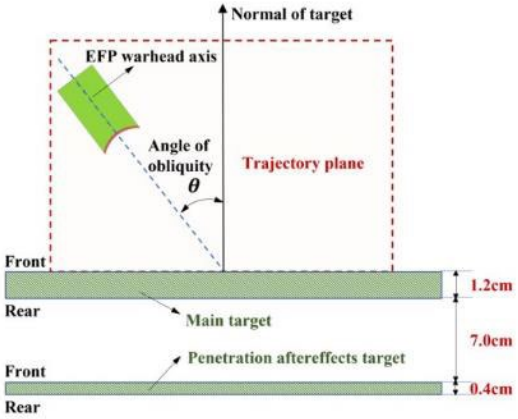

Figure 2 Explosively formed projectile (EFPs) penetrating 6061 aluminum target plate models at different incidence angles

3. Experimental Results

The EFP oblique penetration experiments with different incidence angles showed that with the increase in the incidence angle, the entrance aperture of the main target plate basically increased, and the entrance shape gradually changed from circular to elliptical, as shown in Fig. 3. The length of the short axis of the elliptic hole was basically unchanged at 2 cm, and the length of the long axis of the elliptic hole was the smallest when θ = 15°, with a value of 1.734 cm. The maximum value, 3.27 cm, occurred at θ = 45°. At the same time, there were uneven craters around the entrance caused by the collision between the EFP tail fin and the target plate, and irregular marks were produced by the detonation products on the target plate. For different incidence angles, on both the front and back sides of the plate, there was a flanging phenomenon. For the back side, the flanging shapes were also significantly different for the different incidence angles, and flanging occurred along the left end of the EFP incidence direction. The shape change of the exit was similar to that of the entrance, except for θ = 45°, where the long axis length of the exit was slightly greater than that of the entrance. As shown in the perforation profile in Fig. 4, the penetration aperture decreased first and then increased along the direction of the thickness of the target plate, and irregular necking fracture occurred at the exit.

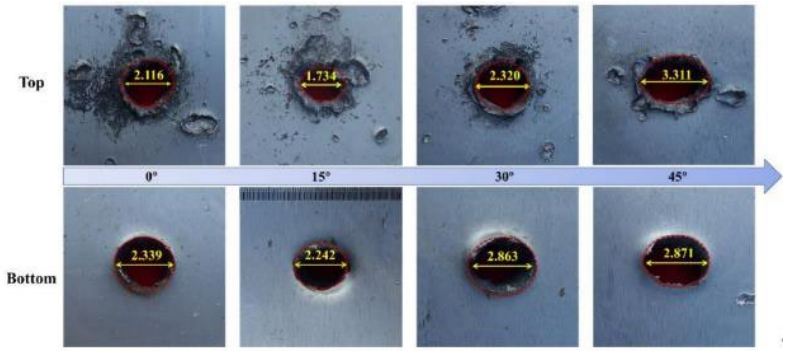

Figure 3 Influence of incidence angle on EFP penetration aperture (unit: cm)

The morphological characteristics of the 6061 aluminum target perforated by the copper EFP high-speed impact were analyzed in terms of two failure modes. Fig. 4 shows typical perforation characteristics of an aluminum target, and Fig. 5 shows SEM images of typical areas. Fig. 4. shows two types of zones visible from the top to the bottom of the target plate for the different incidence angles: the plastic reaming zone and the punching plug fracture zone, and there was a clear boundary between the two zones. The aluminum plate formed a high-temperature and high-pressure zone under the action of the high-speed impact, which led to the melting and erosion of the aluminum in this zone, forming a plastic reaming zone, and the surface was smoother than that of the punching zone. The thrust plug fracture zone was close to the back of the target plate, and necking fracture formed under the action of tension. As Fig. 5 (a) shows, a large melting morphology area appeared on the surface at the entrance of the target plate in the area of intense impact of the projectile target. The thin aluminum target was close to melting in the area of intense impact of the projectile target under the action of the EFP. Fig. 5 (b) shows that in the area where the aluminum target produced punch damage, the main feature of the material failure was self-fracture, which reflected the plastic fracture characteristics of the aluminum target under the action of the EFP high-speed impact.

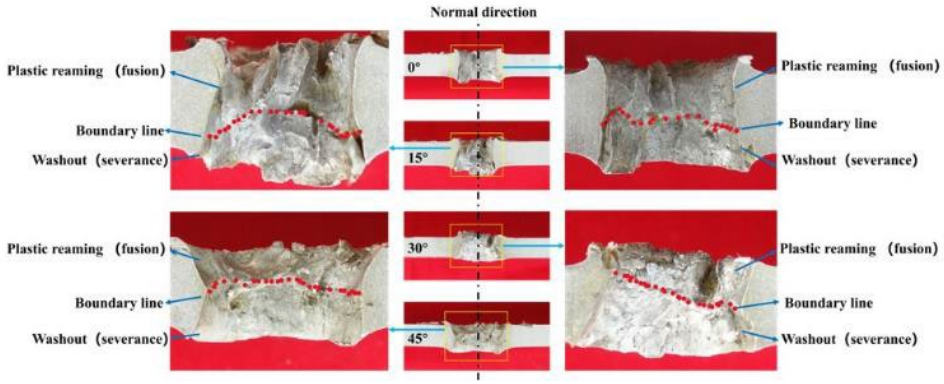

Figure 4 Perforation characteristics of 6061 aluminum targets after EFP high-speed impacts at different incidence angles

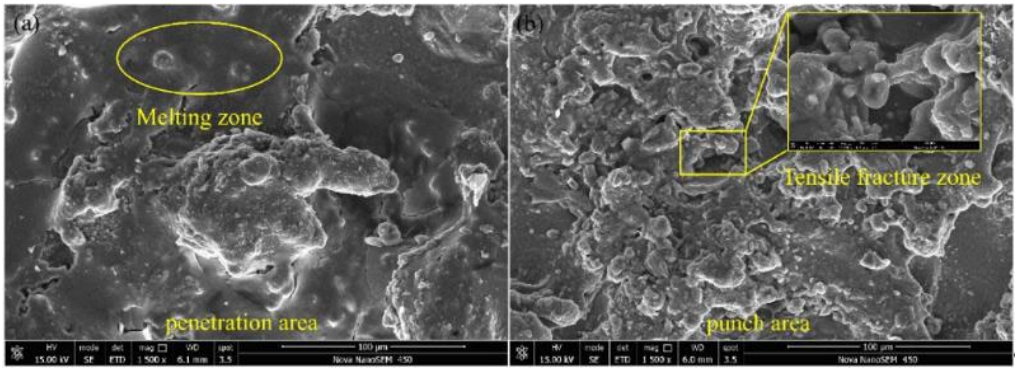

Figure 5 Typical characteristics of EFP highspeed impact aluminum target. (a) penetration area (b) punch area

A large number of studies (Jianping Y 2023, Hu X B 2020, Xing B 2019, Xing B 2019) have shown that an EFP will leave a hole in the target after penetrating it; in other words, the EFP has a strong aftereffect damage ability. The damage state of the aftereffect target in the experiment is shown in Fig. 6. It can be seen from the observation and analysis of the aftereffect plate that the EFP still had a high energy after destroying the aluminum target plate. With the change in the penetration angle, different degrees of damage appeared on the aftereffect plate. After penetrating the thin 6061 aluminum target at different incidence angles, fragments were formed behind the target and collided with the aftereffect plate, and multiple fragment collision points appeared. When the EFP incidence angle was 0°, the aftereffect plate even broke, and there were craters nearby. It can be seen that with the increase in the penetration angle, the fragments behind the target caused decreasing amounts of damage.

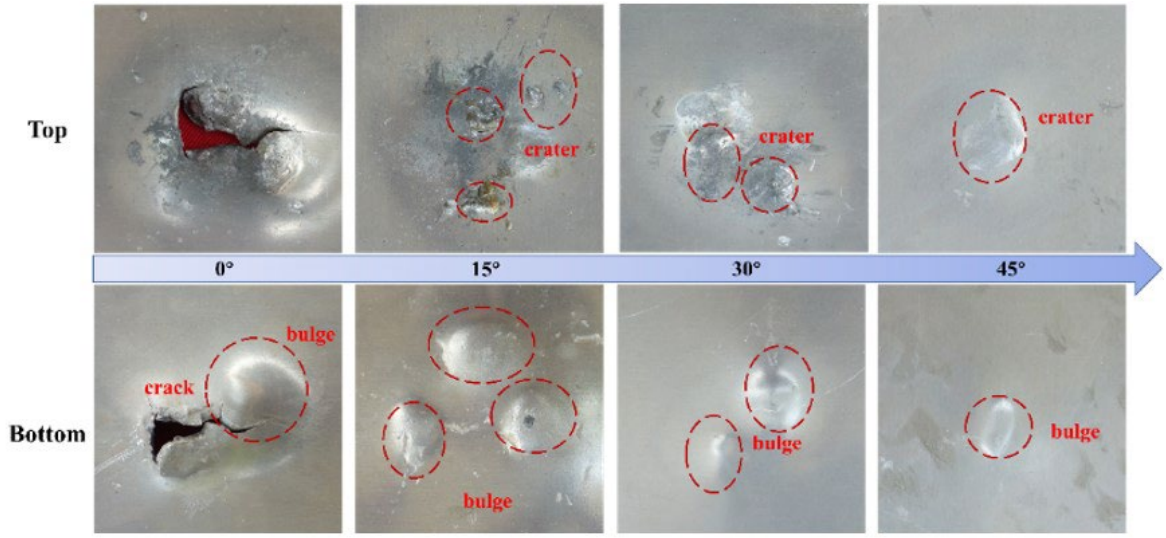

Figure 6 Influence of different incidence angles on the aftereffect of EFPs penetrating the target plate

4. Numerical Simulation Of Copper Explosively Formed Projectile (EFP) Penetrating 6061 Aluminum Target And Failure Mechanism Of Target Plate

4.1 Establishment of simulation model

The formation and penetration of an EFP is a process involving high pressures and strain rates. In order to study the various changes in the process in more detail and reveal the penetration mechanism of the target, the LS-DYNA finite element software was used in this study to simulate the formation process of the EFP warhead and the penetrating process of the metal target. The EFP warhead finite element model is shown in Fig. 7. Due to the symmetry of the object structure studied, only a 1/2 finite element model was established to simplify the calculation. According to the experimental results, there was no evident deformation at the boundary of the target after the impact except for local perforation, which proved that the constraint effect of the bolts in the experimental device on the target plate was successful. Therefore, in order to improve the efficiency of the simulation calculation, solid modeling of the

bolts was not required in the established model, and the constraint effect of the bolts in the model was reflected by applying full constraints to the boundary of the target plate. All the models were based on Lagrangian grids and multifaceted solid units (SOLID164) with eight nodes. The butterfly grid division method was used to divide the liner This grid division could generate a symmetric grid in different parts of the drug-shaped cover, which could better satisfy the numerical calculation requirements. The calculation assumed that the explosive, plastic shell, charge cover, and aluminum target plate were homogeneous continuous media, and the whole explosive penetration process was adiabatic without considering the influence of gravity. The side effects of the target plate were ignored, and the overall motion of the target plate and the influence of air were not considered.

The numerical calculation results showed that the interactions between the detonation product and the powder-type cover had little effect 24 μs after the detonation of the explosive. Therefore, the keywords "*DELETE_PART" and "*DELETE_CONTACT" were added after 24 μs in the numerical calculation to delete the explosive part and the sliding contact between the explosive and the powder-type cover, respectively. A small reboot calculation was performed at the same time. The TrueGrid software was used to generate the grid of the physical model, and the metal and aftereffect targets were subdivided in the regions that were in contact with the EFP. Figs. 7 (c) and (d) show the grid divisions of the aluminum target and the penetrating aftereffect plate, respectively, and the cell dimensions in zone I were 0.08 cm × 0.08 cm × 0.08 cm. The cell dimensions of zone II were 0.08 cm × 0.08 cm × 0.4 cm, and the cell dimensions in zones I and II were 0.4 cm × 0.4 cm × 0. 4 The numerical simulation calculation was carried out using LS-DYNA software, and the units were cm-g-μs.

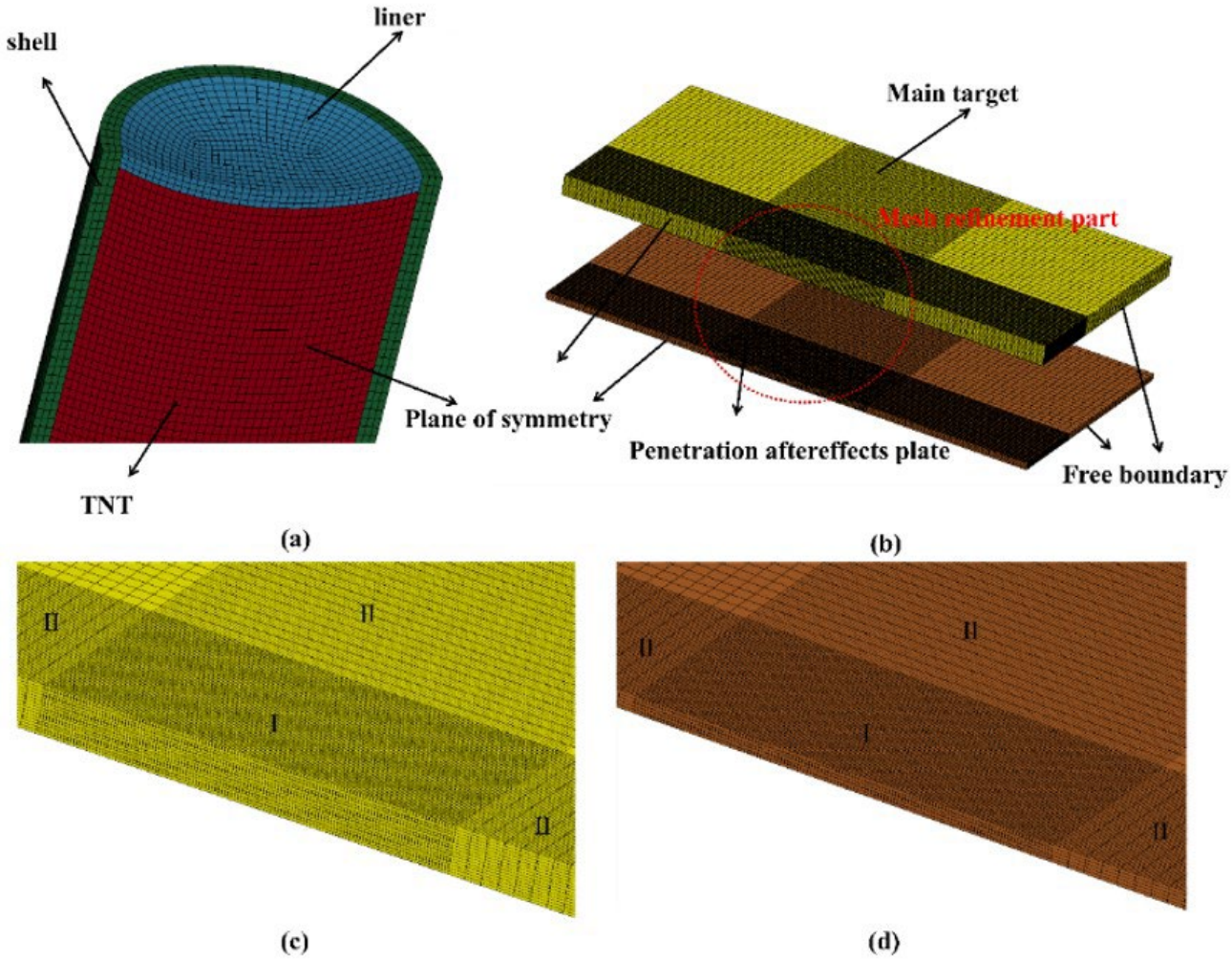

Figure 7 Finite element model: (a) EFP warhead, (b) primary target and penetrating aftereffect target, (c) primary target, and (d) penetrating aftereffect target

4.2 Material constitutive model and parameters

The charge was simulated using the LS-DYNA numerical calculation software. The charge contained in the warhead was described by a constitutive model for high explosives, *MAT_HIGH_EXPLOSIVE_BURN, and the Jones–Wilkins–Lee (JWL) equation of state was used. The JWL equation of state is as follows:

$$P = A(1-\frac{\omega}{R_1V})e^{-R_1V} + B(1-\frac{\omega}{R_2V})e^{-R_2V} + \frac{\omega E}{V} \tag{1}$$

Where ρ is the density, P represents the instantaneous pressure generated after the explosion, which is usually referred to as the detonation pressure, E is the internal energy per unit volume, and V is the relative volume. The state parameters A, R1, B, R2, and ω represent empirical constants, which were obtained by observing and calibrating a large number of explosive initiation experiments. Table 1 shows the parameters related to the explosives.

Table 1 Explosive parameters(Ambrosini D 2020)

ρ/(kg·m−3)	D/(m·s−1)	P/GPa	A/GPa	B/GPa	R1	R2
1658	6930	21	373.77	3.73471	4.15	0.9

To accurately describe the dynamic response of the metal charge cover under an explosion impact, the process of circumferential impact of the detonation wave on the extrusion of the plastic shell and the failure modes at high temperatures, pressures, strains, and strain rates during the high-speed impact of the metal target were examined. The Johnson–Cook (J-C) material model was used to describe the dynamic behavior of the metal drug shield, main target, and penetrating aftereffect target. The yield stress value of the material in the J-C model is

$$\sigma_y = (A_1 + B_1(\bar{\varepsilon}^P)^n)\left(1 + C\ln\dot{\varepsilon}^*\right)(1-(T^*)^m) \tag{2}$$

Formula (2) contains five material parameters, A1, B1, C, n, and m, which were determined by experiments. A1 represents the yield stress constant of the material under small-strain conditions, B1 represents the strain hardening coefficient of the material, n represents the strain hardening index of the material, C represents the strain rate coefficient of the material, and m represents the temperature coefficient of the material. Therefore, the content distribution of the three brackets in the J-C model reflects the strain hardening properties, strain rate hardening properties, and thermal softening properties of the material under isothermal conditions. is the equivalent plastic deformation of the material, is the dimensionless effective plastic strain based on the initial strain rate, T represents the current temperature of the material, Troom represents room temperature, Tmelt represents the temperature at which the material is melted, and T* = (T−Troom)/(Tmelt−Troom) represents the defined relative temperature. The material parameters and equations of state involved in the numerical calculation are shown in Tables 2 and 3. The value ranges of the material parameters were selected based on previous publications (Ambrosini D 2020,Deshpande V M 2022).

Table 2 Main parameter values for the copper Johnson-Cook material model

materials	ρ/(g/cm3)	G/(GPa)	A1/(GPa)	B1/(GPa)	C	m	Tm/(K)	Tr/(K)	Cv
Cu	8.968	46	0.9E-3	2.92E-3	0.025	1.09	1356	300	2.83E-6
6061Al	2.703	28	0.0032	1.14E-3	0.002	1.34	932	300	8.9E-6

Table 3 Parameters of the copper Gruneisen equation of state

materials	C1	S1	S2	S3	γ0	α
Cu	0.394	1.489	0	0	2.02	0.47
6061 Al	0.524	1.338	0	0	2.0	0

4.3 Comparison of experimental results with numerical simulation

Fig. 8 shows the changes in the shape, internal stress, velocity, and length–diameter ratio of the capsule at different times. According to detonation wave theory, at t = 0 μs, after the charge was detonated by the detonator located in the center, a spherical detonation wave formed and was transmitted steadily along the charge, first propagating to the shell. The plastic shell was broken under the combined action of the detonation products and the shock wave. At t = 6 μs, the detonation wave propagated to the bottom of the charge, and the shock wave and detonation products strongly impacted the charge-type casing. In the range of 6–16 μs, due to the difference in the impact effect of each part of the drug cover, the drug cover had a certain velocity gradient in the radial and axial directions under the impact effect, and the velocities of the elements were different. Finally, the material at the top of the drug cover was turned over to form the head of the EFP, and the part at the edge of the drug cover was turned over to form the tail of the EFP. During this process, the axial velocity increased rapidly. When t = 24 μs, the explosive unit was deleted and restarted, and the velocity reached the maximum at this time, with a value of 1210 m/s. After that, the EFP velocity remained unchanged. Due to the velocity difference between the head and the tail fin, the overall length of the projectile was continuously lengthened, and the radial length was continuously reduced under the action of stretching. After 148 μs, a stable EFP had formed with a length–diameter ratio of 1.143and a stable kinetic energy of 17600 J.

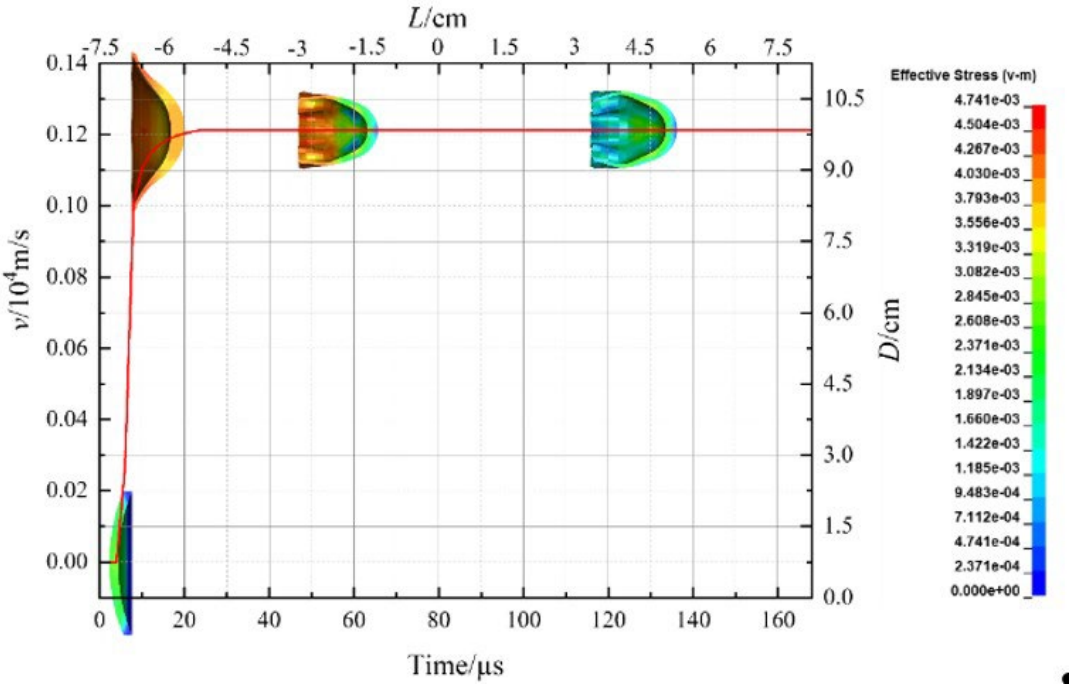

Figure 8. Formation process of EFP

As a shaped energy penetrator that converts a large amount of chemical energy into kinetic energy by an explosion, the EFP mainly relies on its kinetic energy to create damage modes such as perforation, plugging, and lamination. The numerical results of the penetration process of thin 6061 aluminum targets under the high-speed impacts of EFPs at four incidence angles are shown in Fig. 9. According to Birkhof's (2015) penetration theory on the impact of a long cylinder on a metal target, when a projectile hits a finite target at a high speed, transverse plastic flow is generated around the head of the projectile, and with the increase in the penetration depth, the projectile residue will flow from the bottom of the projectile to the edge of the projectile. The target material away from the interface will prevent this flow trend. As shown in Fig. 9. When t = 176 μs, the head of EFP was in contact with the 6061 aluminum sheet, forming stress waves in the projectile and the target plate. When t = 180 μs, the spherical stress wave reached the bottom of the target plate and formed a reflected tension wave. With the increase in the penetration depth, the head of the EFP was deformed when t = 184 μs, the projectile target had a violent effect, the target plate was eroded significantly, and the back of the EFP appeared convex. At the incidence angle of θ = 0° and t = 196 μs, the aluminum thin target began to shrink due to the elastic–plastic deformation of the crater bottom caused by severe stretching. When the tensile strain exceeded the bearing capacity of the target material, the target material fractured and formed a plug block. With the increase in the incidence angle, the time of the necking phenomenon was relatively delayed.

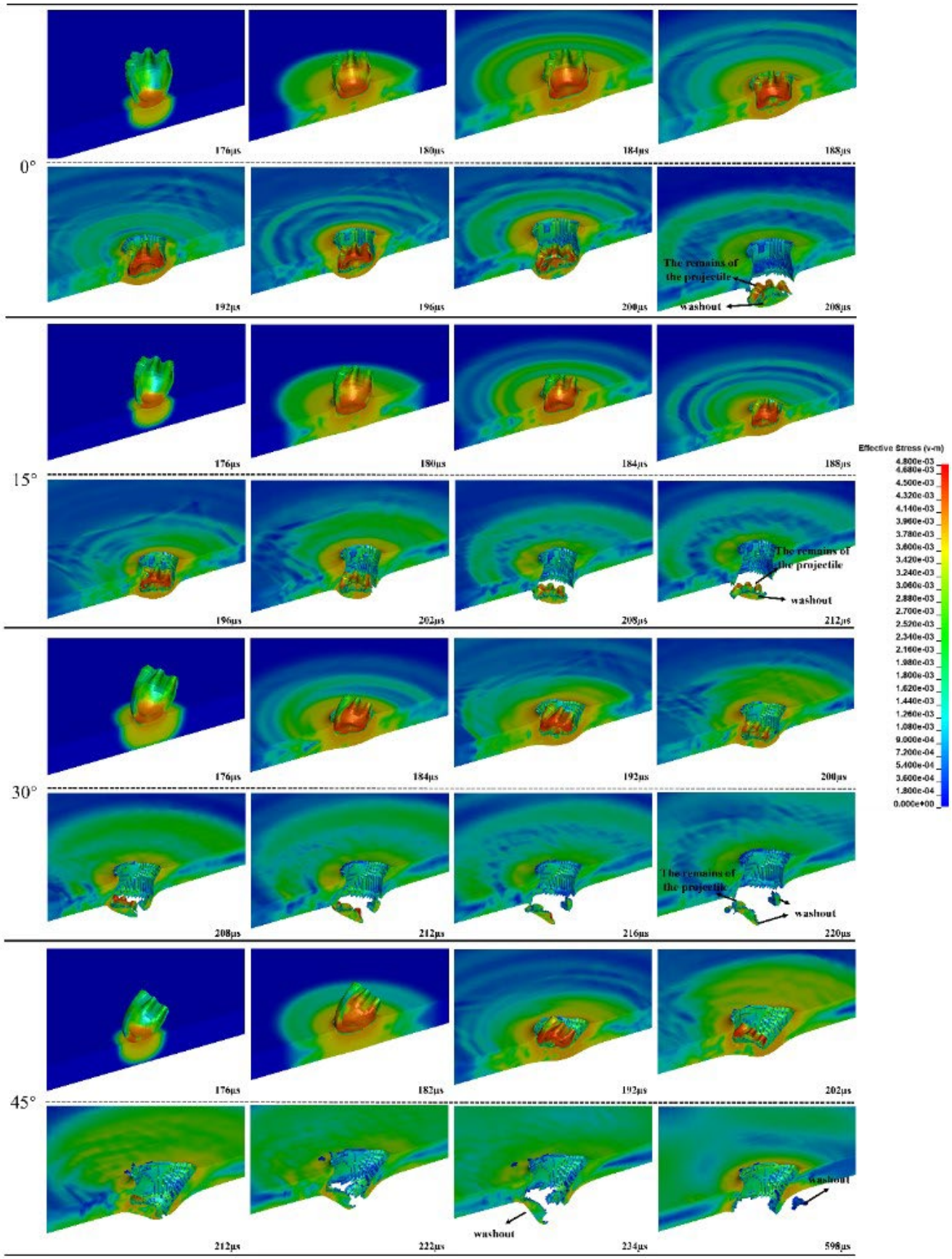

Figure 9 Schematic diagram of the high-speed impact process of a metal aluminum target by an EFP

Based on the schematic diagram of the aperture parameters shown in Fig. 10, the inlet and outlet holes of the metal target at different penetration angles were measured. Combined with the experimental photographs and the aperture data in Table 4, it can be seen that the front side was flanged when penetrating the metal aluminum plate, and the penetration aperture was small for the inlet hole and large for the outlet hole. It can be seen that the experimental results were similar to the simulation results under vertical and other oblique penetration conditions, indicating that the simulation model and material parameters established in this study could relatively accurately reflect the miter penetration problem to be studied.

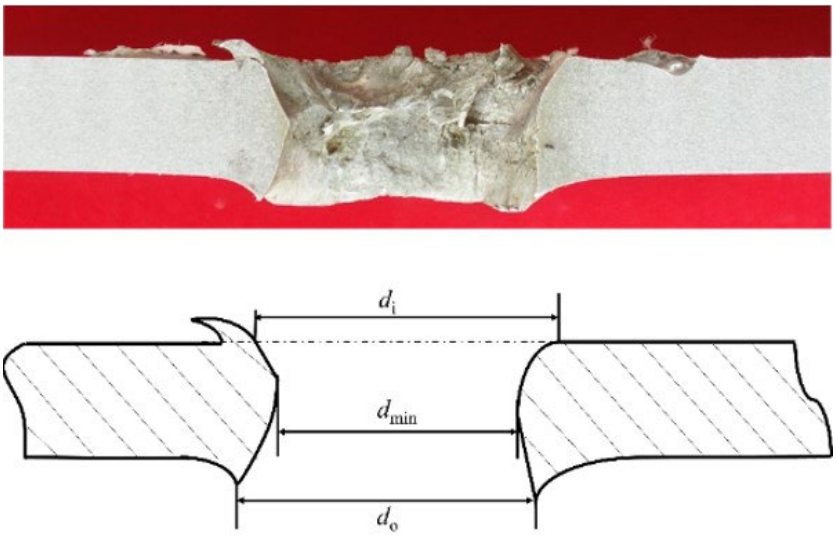

Figure 10. Schematic diagram of aperture parameters of aluminum target perforation

Table 4 Statistical table of perforation aperture

angle	parameters	experimental result/cm	numerical simulation/cm	relative error
0°	d_i	2.116	2.048	3.166%
	d_{min}	2.065	1.886	8.668%
	d_o	2.339	2.174	7.084%
15°	d_i	1.734	2.144	23.644%
	d_{min}	1.768	1.983	12.161%
	d_o	2.242	2.346	4.683%
30°	d_i	2.320	2.527	8.922%
	d_{min}	2.318	2.213	4.529%
	d_o	2.863	2.576	9.989%
45°	d_i	3.311	3.317	0.184%
	d_{min}	2.625	2.852	8.571%
	d_o	2.871	2.706	5.747%

4.4 Failure mechanism and aftereffect

When the incidence angle was present, the EFP had a partial velocity parallel to the plane of the target plate. With the increase in the incidence angle, the partial velocity parallel to the plane of the target plate increased, while that perpendicular to the target plate decreased, and the penetration time increased, resulting in an increase in the aperture of the penetration hole. The EFP penetration process could be roughly divided into three stages.

The first stage was the plastic flanging stage of the target plate (pit opening stage), in which the EFP head first impinged on the target plate. At this stage, due to the very high speed of the EFP head, a plastic deformation area quickly formed around the target plate when the EFP head impinged on the target plate, as shown in Fig. 11. In the first stage, under the action of the projectile pressure, the metal at the intersection of the projectile target complied with the minimum pressure criterion. It mainly flowed out in the opposite direction of the projectile, causing flanging around the entrance port of the target plate.

As shown in Fig. 11 (a), when the EFP was vertically incident, the stresses at each point of the target plate on both sides of the direction of travel were basically the same; however, with an incidence angle, as shown in Fig. 11 (b), the stress at each point of the target plate on the right side in the direction of travel of the projectile was less than that at each point on the left side due to the velocity component parallel to the target plate of the EFP at θ = 30°. According to the minimum pressure criterion, the flanging of the right side of the target plate was more significant than that of the left side.

The second stage was the "righting" stage of the projectile (plastic rear-expanding stage), in which the EFP entered the stable penetration stage, lateral displacement was generated at various points inside the target plate by the extrusion of the projectile, and the rear of the EFP continued to penetrate in the head penetration area and produced a high temperature, which greatly weakened the aluminum target plate and significantly reduced the shear resistance along the thickness direction of the target plate. This was beneficial for the formation of a target plate punch body. When the EFP obliquely penetrated the target plate, the stress state between the EFP and the target plate was more complex than that of the vertical incidence angle. Because the surface of the mushrooming head of the EFP was not flat and the curvatures of the points on the head were different, during the process of the EFP obliquely penetrating the target plate, there was not only resistance from the target plate but also a moment when the projectile began constantly righting itself due to its changing size. As shown in Fig. 11b, the incidence angle of the projectile was θ. After the penetration, the deflection angle of the residual projectile when leaving the target plate was α. Therefore, the target plate caused a θ−α change to the travel direction of the projectile during the whole miter penetration process.

The third stage was the sluicing stage of the target plate. Due to the decrease in the shear resistance of the target plate and the decrease in the penetration kinetic energy, when the thickness of the unpenetrated part of the target plate was thin enough, under the action of the residual kinetic energy from the inertia of the EFP, the target plate in the impact zone of the projectile target was washed out, and a sluicing body with a certain speed was formed. The direction of metal movement around the bullet hole was consistent with the direction of punch movement, causing flanging. After the penetration was complete, the EFP was broken into small pieces of varying sizes, and the EFP residue was tightly combined with punch The punch body and EFP residual shrapnel could improve the ability to cause a certain amount of subsequent killing (aftereffect) of a target behind the armor to a certain extent.

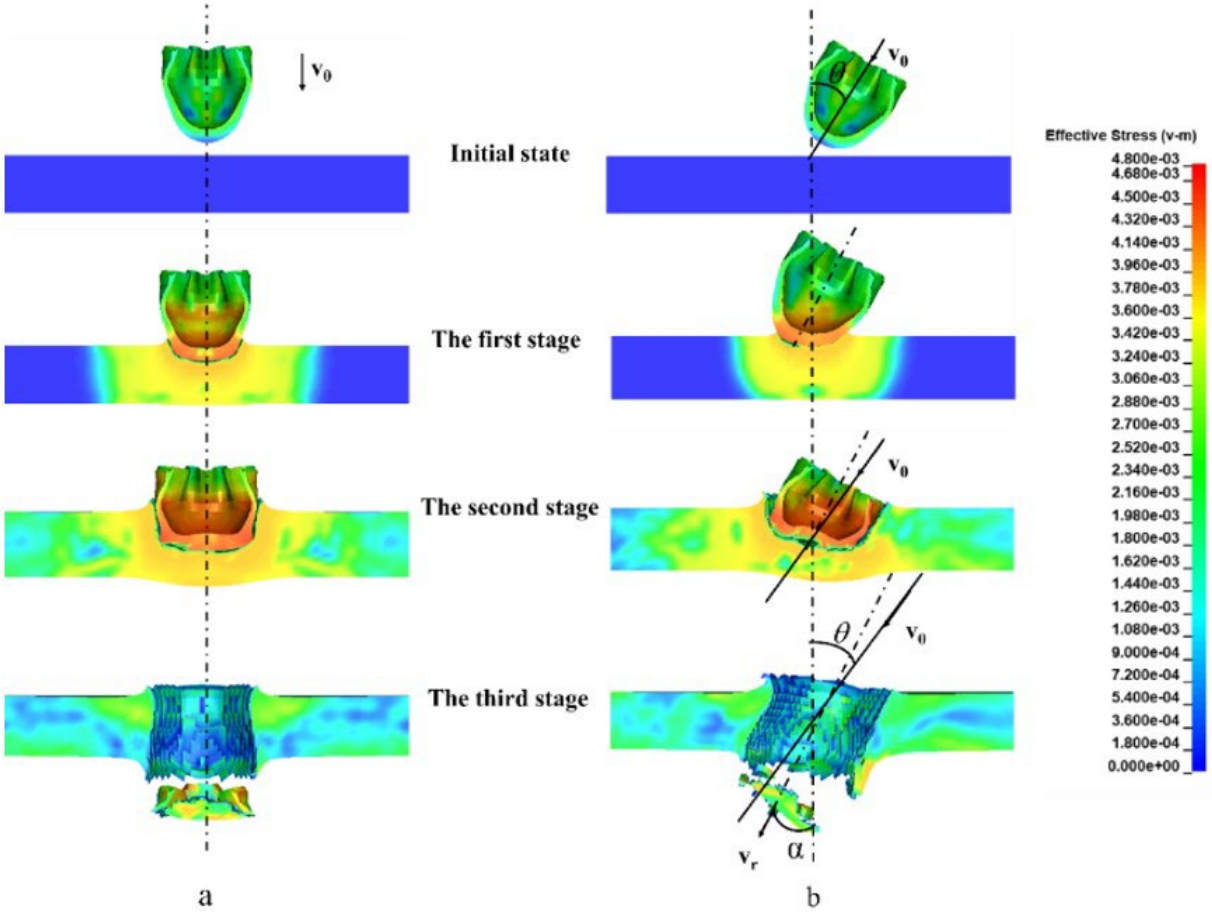

Figure 11 EFP penetration process diagram: (a) vertical penetration and (b) oblique penetration

According to Figs. 8, Fig. 11, and Fig. 12, the stable formation stage of the EFP was within 24 to 176 μs, during which no external forces acted, the velocity was 1210 m/s, and the kinetic energy remained unchanged at 8800 J. During the pitting stage from 176 to 183 μs, the kinetic energy changes of the EFP under the four different angles were basically the same, and roughly 1/4 of the kinetic energy was consumed during the pitting process, during which the EFP squeezed the target plate and produced plastic deformation. The phase of penetration and re-enlargement occurred from about 183 to 199 μs, and the kinetic energy consumption in this process was larger than that in the other two stages, accounting for about 1/2 of the kinetic energy of the whole EFP. The minimum kinetic energy consumption was 38.6% when the incident angle was 0°. When the incidence angle was 45°, the maximum energy consumption was 4460 J, accounting for 50.68% of the total kinetic energy. The reasons for the difference in the kinetic energy penetration of the EFP under different incidence angles are shown in Fig. 11 (b). The equivalent thickness of the EFP body penetrating the target plate, the penetration resistance, and the consumption of kinetic energy increased with the increase in the incidence angle. The third stage occurred from 199 to 216 μs. The target plate at this time was thinner than it was in the first two stages, so the resistance to the projectile was lower, and the kinetic energy consumption rate was significantly lower. At the incidence angle of 45°, the kinetic energy of the EFP was all consumed when it penetrated the first layer of the 6061 aluminum target.

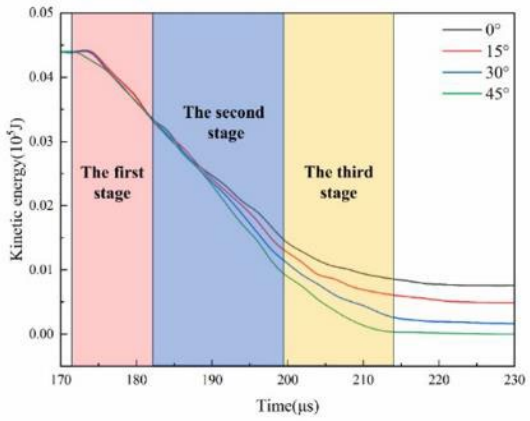

Figure 12 Change in kinetic energy during EFP penetration

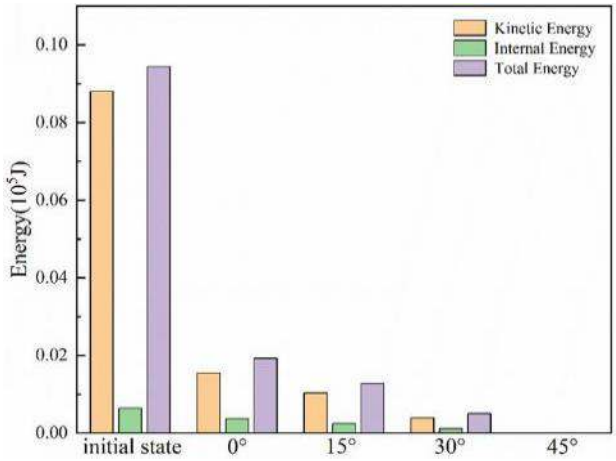

Figure 13 Change in the EFP energy before and after the main target plate penetration

When an EFP, whether vertical or with a certain incidence angle, penetrated the thin aluminum target plate, there were usually residual EFP fragments and punch blocks. Fig. 13 shows the energy change of an EFP after penetrating the main target plate, and Fig. 14 shows the energy absorbed by the aftereffect plate as a representation of the damage effect of the fragments on the penetrating aftereffect plate. When the incidence angle was 0°, the maximum aftereffect was 530 J. With the increase in the incidence angle, the energy absorbed from the EFP residual projectile and punch block decreased—that is, the aftereffect decreased with the increase in the incidence angle. This was consistent with the conclusion obtained for the penetration of the main target plate described above. When the incidence angle was small, the energy consumed by the penetration of the main target plate was small, while the energy absorbed by the aftereffect plate (aftereffect) was large.

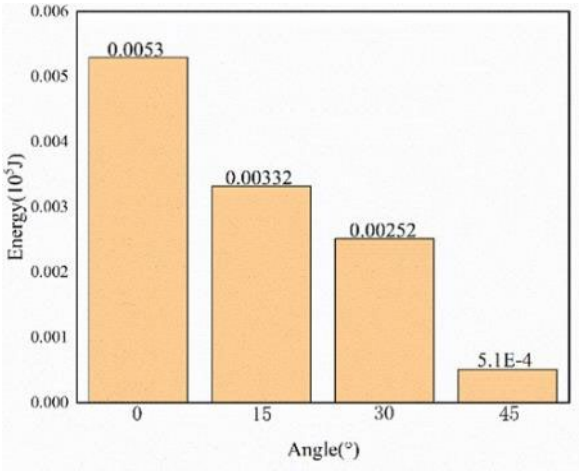

Figure 14 Kinetic energy absorbed by penetrating the aftereffect plate

5 Influence of Penetration Angle on Ballistic Performance And Aftereffect of EFP

To further explore the influences of the different incidence angles on the EFP penetration into the target plate, six other incidence angles were used in the simulations: 5°, 10°, 20°, 25°, 35°, and 40°. Fig. 15 shows the processes of the EFPs penetrating thin aluminum targets under these six conditions. Based on the perforation parameter diagram shown in Fig. 10, the post-processing software was used to measure the relevant dimensions. The results for incidence angles of 0°, 15°, 30°, and 45° are plotted in Fig. 16. The penetration perforation size increased with the increase in the incidence angle. di and dmin were linearly correlated with the incidence angle. For the outlet size do, the size curve was stepped, but the overall trend did not change.

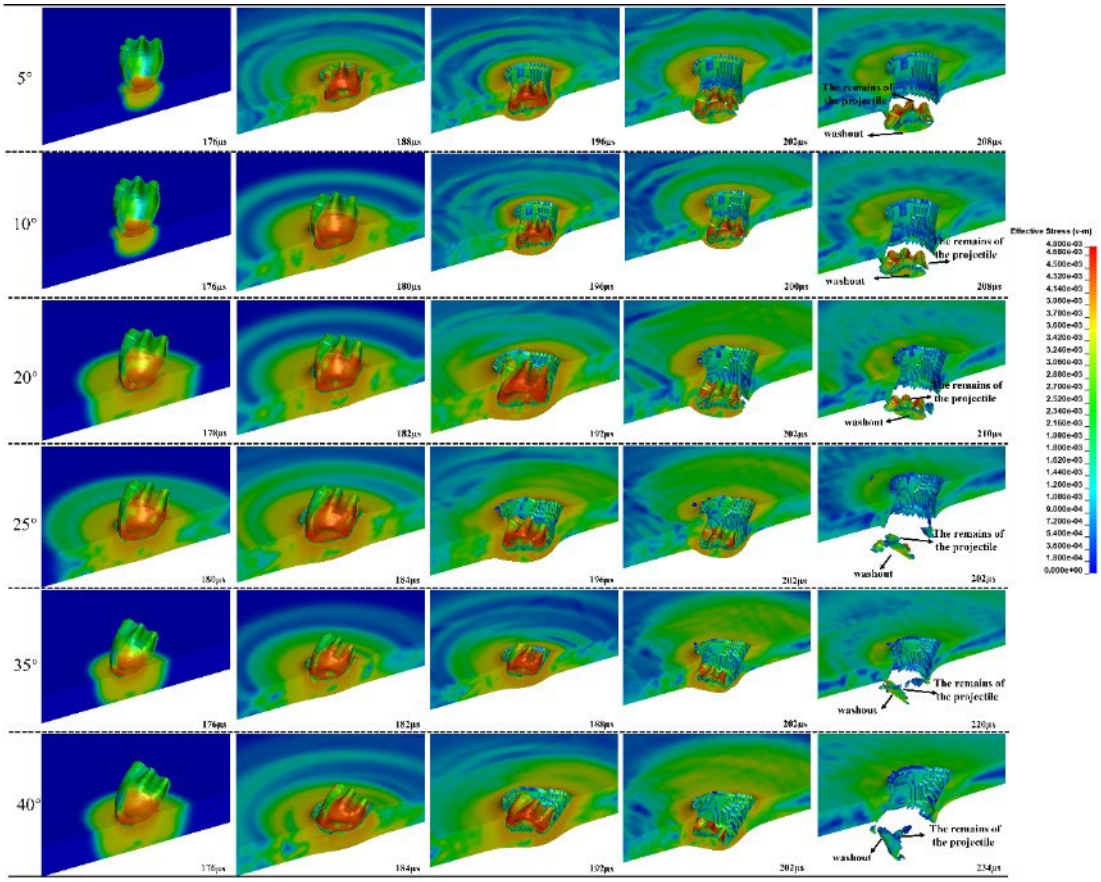

Figure 15 Process of EFP high-speed impact of aluminum target

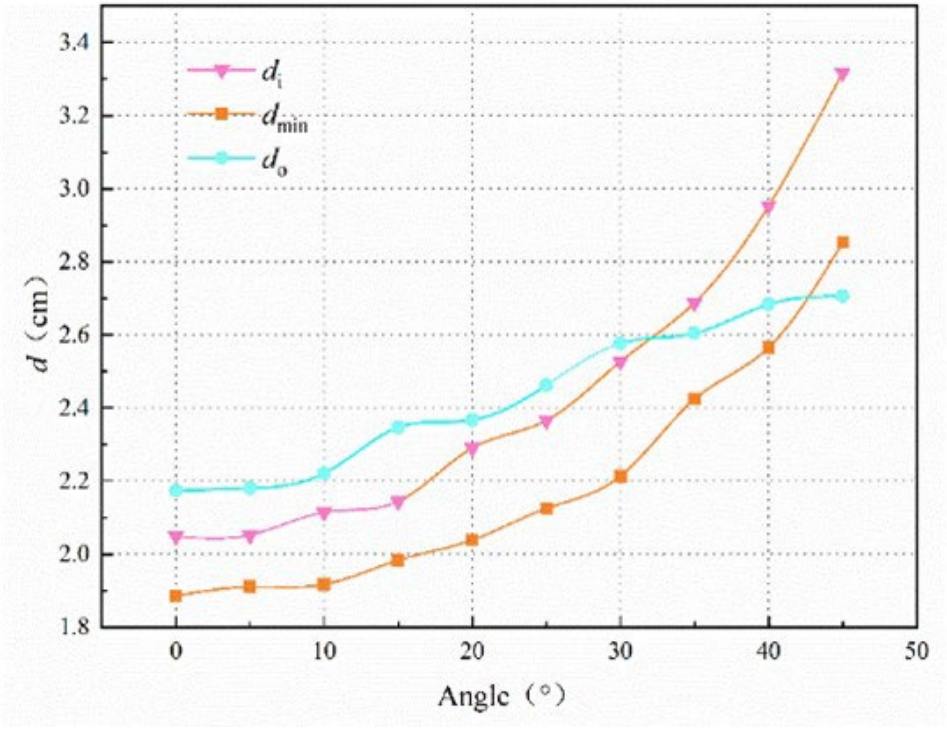

Figure 16 Change in penetration perforation size with incidence angle

With the change in the incidence angle, the energy absorbed by the 6061 aluminum plate and the aftereffect plate is shown in Fig. 17. It can be seen that the energy absorbed by the aluminum target plate was much higher than that of the aftereffect plate, which was consistent with the result described above. The energy of the EFP was mainly consumed in the penetration of the aluminum target plate, while for the aftereffect plate, the energy came from the debris formed by the residual EFP and the punch. With the increase in the incidence angle, the difference in the amounts of energy absorbed of the first and second layer target plates also gradually increased.

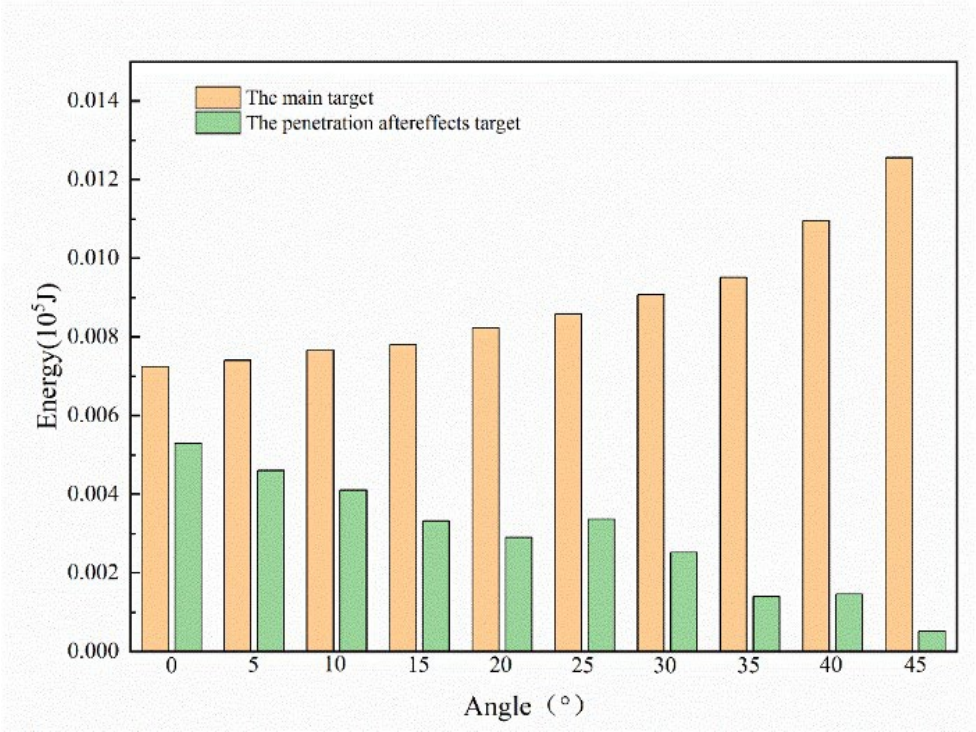

Figure 17 Change in energy absorbed by the target plate with the incidence angle

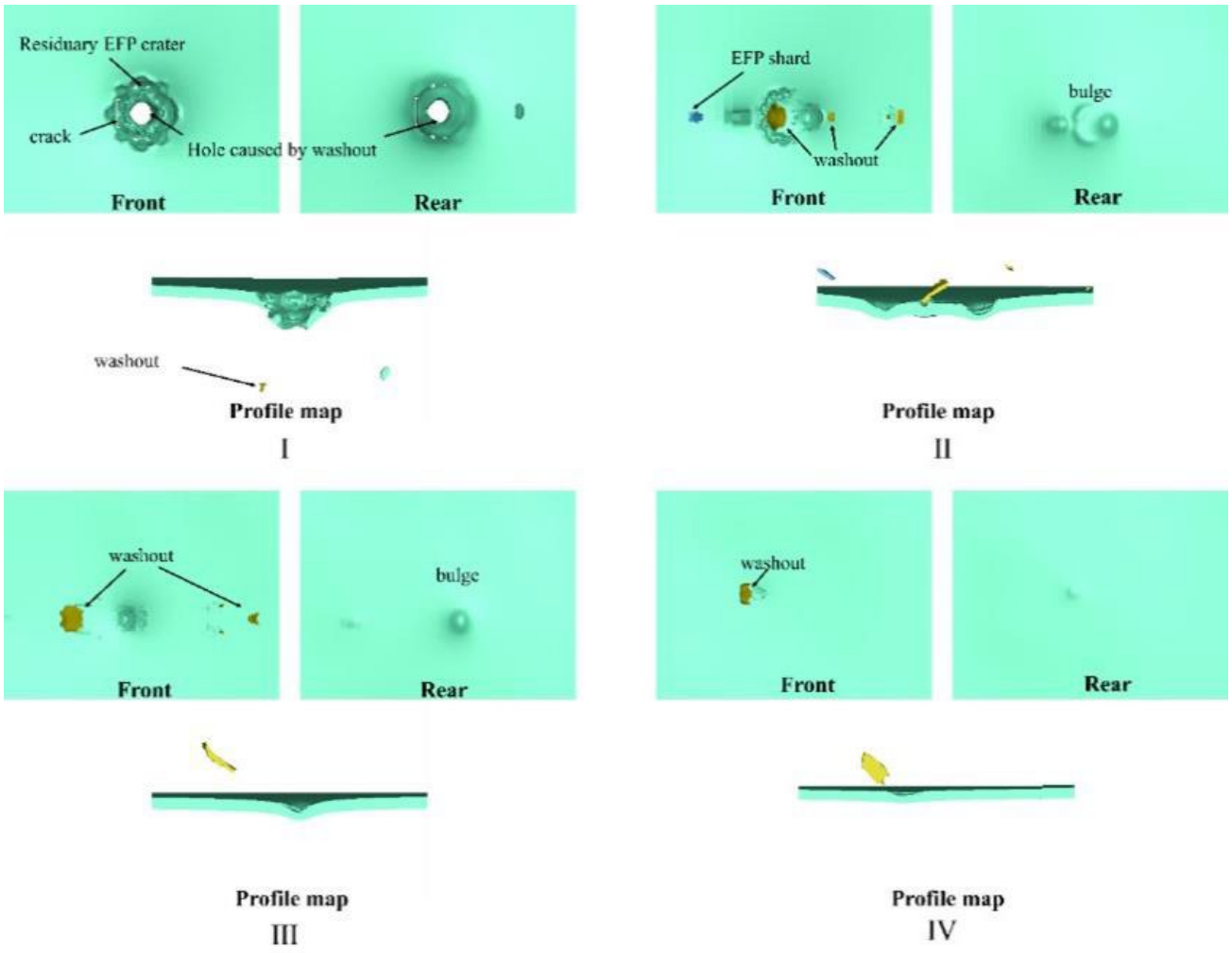

Figure 18 Four damage modes for penetration of aftereffect plates

In this experiment, the damage to the aftereffect plate was mainly from the projectile fragments and the punching block generated by the EFP penetrating the aluminum sheet due to its own continuous erosion and damage. In order to show the damage grade of the aftereffect for different incidence angles, four aftereffect damage modes, labeled I–IV, were proposed based on the damage degree of the aftereffect plate. Fig. 18 shows the damage schematic diagram of the four modes.

Damage mode I: After the residual EFP and punch block hit the aftereffect plate, due to the large kinetic energy, high tensile and shear stresses are formed at the impact point. Once the critical failure stress of the aftereffect plate is exceeded, cracks or perforations will be formed, and cracks will continue to expand under the action of inertia.

Damage mode II: The residual EFP and punch block do not have large kinetic energies, and they can only form a crater on the aftereffect plate and a large bulge on the back side. In this state, there is a large angle between the velocity direction before the collision and the normal direction of the aftereffect plate, and a ricocheting phenomenon may occur after the first collision.

Damage mode III: The EFP is completely eroded in the process of penetrating the aluminum sheet, or the residual EFP has a small kinetic energy and has no evident effect on the aftereffect plate. Therefore, in this mode, only the punch block can cause damage to the aftereffect plate. Under the action of the punch block, the aftereffect plate forms a crater with a significant protrusion on the back.

Damage mode IV: In this mode, the kinetic energy of the punch block is relatively small, and no evident pits are formed when it collides with the aftereffect plate.

According to the above description of the damage modes of the aftereffect target plate, the damage modes of the aftereffect target plate under ten operating conditions with an incident angle ranging from 0° to 45° were classified, as shown in Fig. 19. The figure also includes the kinetic energies of the fragments and the changes in the energies of the main target plate and the aftereffect target plate during the penetration processes at different incident angles.

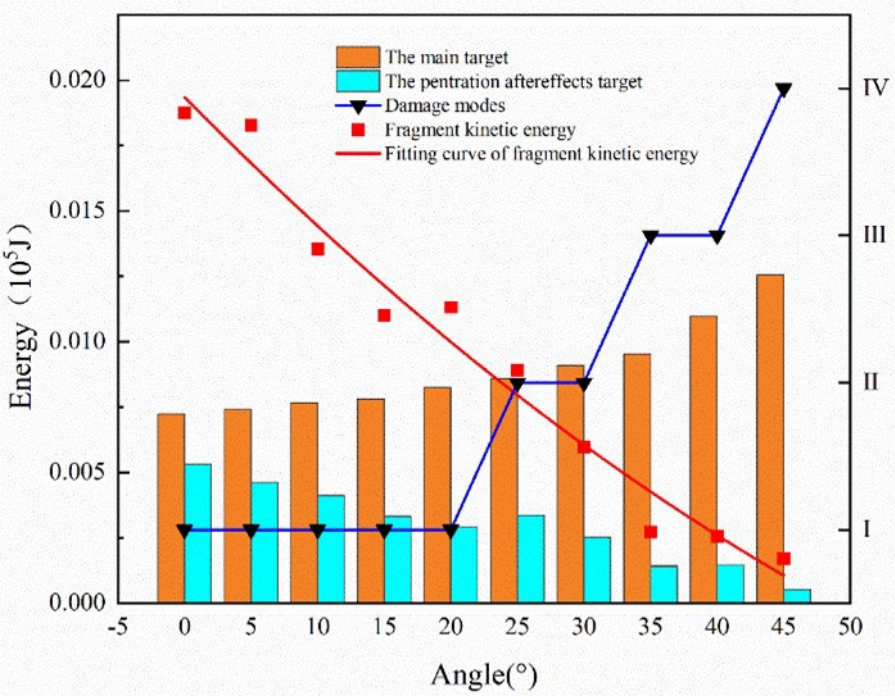

Figure 19 Damage grade diagram at different incidence angles

It can be seen that when the incidence angle θ ranged from 0° to 20°, the residual velocity changed little, which indicated that the oblique penetration of the EFP was insensitive to the change in the incident angle at small inclination angles. The aftereffect effect was larger at a small inclination angle, and the damage mode of the aftereffect plate was mode I. When the incidence angle changed from 25° to 40°, the damage mode changed from mode II to mode III. When the incidence angle θ increased from 40° to 45°, the residual velocity decreased significantly, and the damage mode changed from mode III to mode IV. It can be seen that under the condition of a large incidence angle, the aftereffect of the EFP penetrating the 6061 aluminum sheet was minimal.

6. Conclusions

In this study, the penetration performances of EFPs on thin 6061 aluminum targets at different incidence angles were studied. Based on the analysis of the damage mechanism and the comparison of the energy changes and penetration results between the projectile and target plate, the following conclusions were drawn:

1. The process of an EFP plastic projectile penetrating a 6061 aluminum sheet was roughly divided into three stages, namely the target plate plastic flanging stage, the projectile righting stage, and the target plate punching stage. In the process of penetrating the thin 6061 aluminum target plate, the energy consumed in the second stage was relatively large, and the energy consumed was the largest at a 45° incidence angle, reaching 50.68% of the energy required for penetration.
2. In the area where the projectile target had a strong effect, the surface of the entrance of the target plate exhibited a large area with a melting morphology. This indicated that the aluminum target was close to melting in the area where the projectile target had a strong effect under the EFP impact. In the area where the aluminum target produced punch damage, the main feature of the material failure was fracture. This revealed the brittle fracture characteristics of the 6061 aluminum target under the EFP high-speed impact.
3. The aftereffect of the EFP mainly came from the residual EFP fragments after penetrating the first layer of the target plate and the punch block formed by the completion of the penetration. The aftereffect was also reflected in the kinetic energies of these fragments. With the increase in the incidence angle, the aftereffect also decreased.
4. When the incidence angle θ ranged from 0° to 20°, the residual velocity changed little, and the damage mode of the aftereffect plate was mode I. When the incidence angle changed from 25° to 40°, the damage mode changed from mode II to mode III. When the incidence angle θ increased from 40° to 45°, the residual velocity decreased significantly, and the damage mode changed from mode III to mode IV.

Acknowledgments

This research was supported by the National Natural Science Foundation of China, Grant Nos. 12202497 and 12102479. The authors would like to gratefully acknowledge this support.

Author's Contribuitions: Writing - original draft, Yuxuan Gao; Test technical support, Chong Ji, Yuting Wang, Xin Wang; Writing - review & editing, Changxiao Zhao; Numerical simulation technical support, Xin Wang.

Editor: Marcílio Alves

Reference

Ambrosini D, Luccioni B,(2020) Effects of underground explosions on soil and structures. Underground Space 5(4):324-338.

Birkhoff G, MacDougall D P, Pugh E M, et al.(1948)Explosives with lined cavities. Journal of Applied Physics 19(6):563-582.

Cheng C, Fu Y, Du C, et al.(2022) Oblique penetration law of short-rod projectile into thin metal target. Mechanics of Advanced Materials and Structures 1-12.

Heberling T, Terrones G, Weseloh W,(2018) Hydrocode simulations of a hypervelocity impact experiment over a range of velocities. International Journal of Impact Engineering 122:1-9.

Heberling T, Terrones G, Weseloh W,(2018) Hydrocode simulations of a hypervelocity impact experiment over a range of velocities. International Journal of Impact Engineering 122:1-9.

Hu X B, Wang C T, He Y, et al.(2020) Investigation on formation process of a Ta-based dual phase alloy EFP liner. In Journal of Physics: Conference Series 32-33.

Ji C, Chen L, Long Y, et al.(2015) Dynamic behaviors of multi-layered steel targets with air gaps subjected to the impact of EFP simulants. International Journal of Protective Structures l6(1): 65-80.

Jianping Y, Yakun L, Zhijun W, et al.(2023) Formation and penetration of PELE/EFP multi-mode warhead based on double-layer shaped charge. Journal of Energetic Materials 41(1):4-26.

Kurzawa A, Pyka D, Bocian M, et al. (2018). Metallographic analysis of piercing armor plate by explosively formed projectiles. Archives of Civil and Mechanical Engineering 18:1686-1697.

Lee W S, Lai C H, Chiou S T,(2001) Numerical study on perforation behavior of 6061-T6 aluminum matrix composite. Journal of Materials Processing Technology 117(1-2):125-131.

Li H T, Fei W D, Yang D Z,(2002) Damage of aluminum borate whisker reinforced 6061 aluminum composite under impact of hypervelocity projectiles. Materials Science and Engineering: A 333(1-2):377-379.

Liu J, Long Y, Ji C, et al. (2018). Ballistic performance study on the composite structures of multi-layered targets subjected to high velocity impact by copper EFP. Composite Structures 184:484-496.

Liu J, Long Y, Ji C, et al.(2017). The influence of liner material on the dynamic response of the finite steel target subjected to high velocity impact by explosively formed projectile. International Journal of Impact Engineering 109:264-275.

Manoj G, Sanjay H S, Dinesh P A, et al.(2022) Design and Development of a collapsible wheel for wheelchair-based applications using Aluminum 6061 material. International Applied Mechanics 58(2): 236-242.

Mayén J, Abúndez A, Porcayo-Calderón J, et al.(2017) Part 1: Design and development of new sustainable coatings applied on aluminium 6061 alloy-RRA heat treated for engineering applications. Surface and Coatings Technology 328:488-498.

Vayig Y, Ornai D, Rosenberg Z.(2022) A numerical study on the oblique penetration of spherical-nosed rigid projectiles into semi-infinite metallic targets. Journal of Dynamic Behavior of Materials 8(3):397-404.

Wubieneh T A, Tegegne, S T.(2022) Fabrication and characterization of aluminum (Al-6061) matrix composite reinforced with waste glass for engineering applications. Journal of Nanomaterials.

Xing B, Guo R, Hou Y, et al (2019) The mass distribution of behind-armor debris generated during the normal penetration of variable cross-section explosive formed projectile on rolled homogeneous armor steel. International Journal of Impact Engineering 129:12-25.

Xing B, Zhang D, Guo Z, et al.(2019) Analysis of the mass of behind-armor debris generated by RHA subjected to normal penetration of variable cross-section EFP. Defence Technology 15(3): 390-397.

Yadav B K, Jahangiri M, Singh D,(2022). Experimental and Numerical Simulation to Validate Critical Perforation Velocity on a Flat Plate Aluminium Alloy 6061. Advances in Materials Science and Engineering 1-31.